UV Index from Global Solar Irradiance: performance according to cloudiness and air mass

Agustín Laguarda[1*] and Gonzalo Abal[2]

[1*]Instituto de Física, Facultad de Ingeniería (UDELAR),
Herrera y Reissig 565, Montevideo, 11000, Uruguay.
[2]Laboratorio de Energía Solar, CENUR Litoral Norte (UDELAR),
Luis Batlle Berres km 508, Salto, 50000, Uruguay.

*Corresponding author(s). E-mail(s): laguarda@fing.edu.uy;

Abstract

Ultraviolet (UV) irradiance from the Sun has potential negative health impacts. Erythemal UV irradiance (UV-E) is obtained by weighting UV radiation in the 250-400 nm range with the average skin erythemal response function. UV-E is proportional to the UV Index (UVI), a tool used worldwide to inform the public about this environmental hazard. Since this magnitude is not currently measured at most meteorological sites, satellite based estimates are often used to generate UV-E information over broad areas. However, for a climatological characterization of variability and typical doses of UV-E, long time series with low biases are required. An alternative approach is to estimate UV-E from readily available information with which UV-E is highly correlated. This work builds upon previous research, which evaluated a simple model (Power Model or PM) to estimate UV-E from Global Horizontal Irradiance (GHI), relative air mass, and total atmospheric ozone concentration at the 10-minute level. In that general analysis, the model showed an uncertainty below 12% (as measured by its relative Root Mean Squared Deviation or rRMSD) when compared with ground UV-E measurements. Here, we present a more in-depth assessment of this model, using high-quality data from four mid-latitude temperate sites. The deviations of the model estimates from UVI ground measurements are analyzed under different cloudiness conditions and across a broad range of air masses. Our results confirm that PM performs best under clear skies and low air masses, precisely the conditions associated to the higher incident solar irradiances and potentially dangerous UV levels. Under these conditions, the PM has an average accuracy (rRMSD across sites) of less than 6% of the average of the measurements and outperforms . These results confirm that the model, particularly in its unbiased version, is a reliable and practical tool for the climatological analysis of erythemal UV irradiance.

Keywords: environmental UV radiation, radiation model, erythemal solar irradiance, UV index

1 Introduction

Ultraviolet (UV) irradiance from the Sun represents less than 10% of the total extraterrestrial solar irradiance and most of it is absorbed in the atmosphere. However, the small amount of UV irradiance reaching ground level has important impacts on human health and biological systems and causes degradation processes in exposed plastic materials.

According to the ISO 21348:2007 standard (ISO, 2007), solar UV radiation is categorized into three sub-bands: UV-C (100–280 nm), UV-B (280–315 nm) and UV-A (315–400 nm). The UV-C sub-band, the most energetic and potentially damaging UV radiation, is completely absorbed in the atmosphere mostly by ozone and molecular oxygen. Most of the UV-B band is also absorbed by the atmosphere, but a small and variable amount persists in the ground level solar spectrum. This component is potentially dangerous to human health, enhancing skin aging and significantly increasing the risk of skin cancer. Furthermore, cumulative exposure to environmental UV-B irradiance over extended time periods accelerates the degradation of proteins in the eye and may eventually lead to cataracts (Ji et al, 2015). UV-A is the least energetic UV subband and accounts for approximately 95% of the UV solar radiation at ground level, since it is weakly absorbed in a clear atmosphere. It penetrates into the skin, causing tanning and skin aging. Recent evidence suggests that UV-A may also contribute to skin cancer through indirect mechanisms (Liu-Smith et al, 2017).

1.1 Erythemal UV (UV-E)

The effects of UV irradiance on the human skin are best evaluated taking into account the skin response function which, in essence, defines how much of the incident UV spectral irradiance is absorbed at each wavelength by an "average" skin type. Different skin types have different response functions, so a standarized Erythema action spectrum response function representing the response of an average skin type to UV radiation has been defined in 1998 by the International Commission on Illumination (CIE) and later adopted as an ISO-CIE joint standard (ISO, 1999). This standard erythemal skin response function, $S_{ER}(\lambda)$, is the result of a mathematical fit to experimental data, represented by three straight lines on a logarithmic plot, as shown in Fig. 1(a). It can be parametrized by

$$S_{er}(\lambda) = \begin{cases} 1.0 & \text{for } 250\,\text{nm} < \lambda \leq 298\,\text{nm} \\ 10^{0.094(298-\lambda)} & \text{for } 298\,\text{nm} < \lambda \leq 328\,\text{nm} \\ 10^{0.015(140-\lambda)} & \text{for } 328\,\text{nm} < \lambda \leq 400\,\text{nm} \end{cases} \tag{1}$$

with the wavelength λ expressed in nm (Webb et al, 2011). Since the erythemal skin response in the UV-B range is an order of magnitude higher than in the UV-A range,

even relatively low levels of UV-B exposure, accumulated over time, can significantly impact human health. The erythemal UV solar irradiance (UV-E, in $\mathrm{mW/m^2}$) is defined in terms of the spectral solar irradiance $E(\lambda)$ (in $\mathrm{W/m^2nm}$) as,

$$\text{UV-E} = \int_{280\,\mathrm{nm}}^{400\,\mathrm{nm}} S_{er}(\lambda)\, E(\lambda)\, d\lambda. \tag{2}$$

In Fig. 1(b) the spectral global irradiance in the 300-400 nm range is shown as measured on a horizontal surface by an Eko MS711 spectroradiometer (spectral range: 300–1100 nm). This sample measurement (blue line) corresponds to an early spring day under clear sky conditions at the Solar Energy Laboratory (LES) main facility, in northern Uruguay, used in this work (see Table 2 for the exact location). The black curve corresponds to the standard extraterrestrial irradiance in this range (Gueymard, 2004). The blue curve is the measured spectral irradiance at ground level, $E(\lambda)$ and the green curve is the spectral UV-E, $S_{er}(\lambda)\, E(\lambda)$. A dashed vertical line separates the UV-A and UV-B sub-bands contributions to UV-E. In this example, UV-B contributes about 73% of the UV-E irradiance[1]. The global UV Index (UVI) is used worldwide to communicate and alert the population in simple terms about the health-related hazards associated to exposure to solar UV irradiance. One unit of UVI is equivalent to a UV-E irradiance of $25\,\mathrm{mWm^{-2}}$ (UVI = UV-E/$25\,\mathrm{mWm^{-2}}$) so it is dimensionless and usually below 20. Prolonged exposure to UVI values greater than 8 is not recommended, according to WHO guidelines (World Health Organization, 2002).

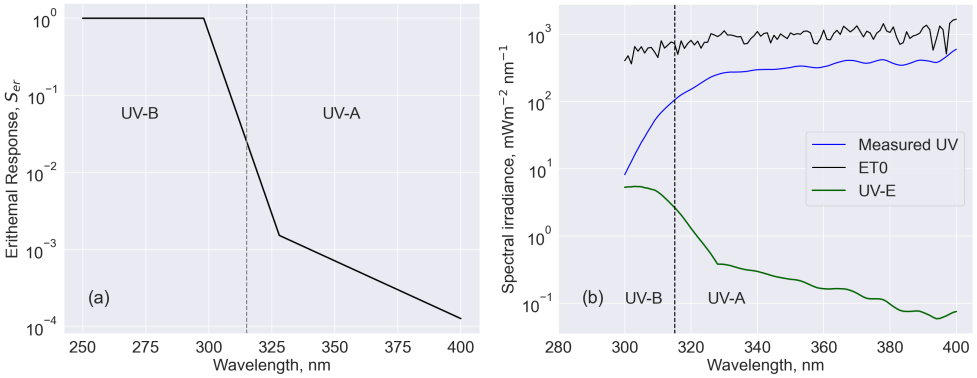

Figure 1 (a) Standard Erythemal response, Eq. (1). (b) Measured global UV Spectral irradiance on a horizontal plane for the LES site (blue) and the corresponding UV-E from Eq. (2) (green). In black, the extraterrestrial standard irradiance (ET0).

Understanding the inter-annual variability of UVI and other climatic characterizations of UV-E, such as daily average doses, is essential for assessing its potential occupational health impacts. However, despite the importance of monitoring UV-E,

[1]The restriction $\lambda > 300\,\mathrm{nm}$ imposed by the measuring apparatus implies that some of the UV-B contribution is not accounted for in this example.

its measurement remains limited. Even though several commercially available instruments can measure environmental UV-E, they require frequent calibration and this magnitude is not currently included in the set of routine measurements maintained by most meteorological stations. Consequently, real-time UVI information is often derived from publicly available satellite-based estimates, which offer global coverage but provide only an approximation to the real conditions at specific locations. An example of this kind of information is provided by the CAMS (Copernicus Atmospheric Monitoring System) UVI product (Copernicus Atmosphere Monitoring Service (CAMS), 2024). On the other hand, ground UV-E (or UVI) measurements, when available, are only representative of a small geographical area around the measurement site.

As for other solar radiation sub-bands, techniques used to model solar UV radiation at ground level can be grouped in three approaches: Radiative Transfer Models (RTM), models that use Artificial Neural Networks (ANN) and empirical (or phenomenological) models. RTMs simulate the interaction of solar radiation with the atmosphere, accounting for absorption and scattering by various atmospheric constituents (Čížková et al, 2018; Arola et al, 2002). They are computationally intensive and can provide spectral information for ground level solar irradiance and its sub-bands, provided the atmospheric composition is known in detail since they are highly sensitive to the accuracy of these inputs. An operational example based on this approach is the UV product from CAMS and the European Centre for Medium-Range Weather Forecasts (ECMWF), which uses a numerical weather model to provide atmospheric information (including cloud cover and its optical properties) and a RTM to estimate surface spectral irradiance, both under clear and all sky conditions (Eskes et al, 2024). A recent validation of this UV product over several sites worldwide (Pitkänen et al, 2020) shows a Root Mean Square Deviaton (rRMSD) of 36% and Mean Bias Deviations (rMBD) in the range ±20%, relative to the average of the measurements (see Subsection 2.2 for the definitions of these metrics). Simplified approaches based on RTMs, such as SMARTS (Gueymard, 2019), use parametrizations to describe scattering and absorption of solar radiation by atmospheric components and can provide ground spectral irradiance, including UV-A and UV-B bands, without being intensive in computational resources. However, these physical spectral models are restricted to clear sky conditions and their accuracy is also limited by the accuracy of the atmospheric information available.

ANN models have been used successfully to estimate ground level UV irradiance (Dieste-Velasco et al, 2023). They require large amounts of local training data (including UV irradiance and environmental and atmospheric data) and provide no physical insight on the relationship between auxiliary variables and UV irradiance. Usually they can perform accurately at one location but require a new training (with all the training data) to reproduce this performance at a different location. Thus, there is a need for alternative methods that allow reliable long-term UVI estimation from more commonly measured meteorological variables. The development of simple yet robust models that estimate UV-E from widely available data sources could enable better climatological studies and health risk assessments, especially in regions where UV irradiance measurements are scarce.

Phenomenological models attempt to simplify the problem of UV estimation using a set of relevant auxiliary variables which are easily available (for instance global horizontal irradiance, ozone column and aerosol density) (Habte and Sengupta, 2020; Laguarda and Abal, 2019; Antón et al, 2008, 2009). Their coefficients will require adjustment to reduce biases, but one set of coefficients can be used over broad areas with similar climates, with acceptable accuracy loss. Since they are (by design) based on easily accessible information, they may be trained easily for any desired location. The choice of the auxiliary variables in a phenomenological model represents a compromise between achieving enough accuracy over the target region without using too many adjustable coefficients which may affect its usability.

The most basic phenomenological model uses measured Global Horizontal Irradiance (GHI) as its single auxiliary variable and assumes a constant UV-E/GHI ratio, thus using a single adjustable parameter. Of course, there are several relevant factors affecting ground-level UV-E irradiance, such as cloud cover, ozone column, air mass (solar altitude), surface albedo, aerosol content and water vapor (Bernhard et al, 2023). The relative importance of each factor will depend on local characteristics, in particular the typical climate. Using GHI as auxiliary variable includes, to some extent, the effects of water vapor or aerosol density. Excluding areas with particular characteristics (such as seasonal snow cover, mountains or deserts) the albedo effects are partially present also in GHI. However, the role of albedo and materials reflectivity must be considered for modeling UV occupational doses under realistic conditions (Turner and Parisi, 2018). Therefore, GHI, air mass and ozone content are a set of auxiliary variables which represent a good compromise between accuracy and simplicity when modeling global horizontal UV-E at ground level.

1.2 Objective of this work

As mentioned, several linear and non-linear UV irradiance models have been proposed and evaluated using GHI, air mass and ozone concentration as input information. In a recent work (Laguarda et al, 2024) we explored the performance of different phenomenological parametrizations for modeling UV-A, UV-B and UV-E from these variables using data for five temperate mid-latitude sites. The best model for UV-E was based on a product of power functions in these variables, thus the name 'Power Model'. This model was first proposed in Antón Martínez (2007); Antón et al (2008) and tested in areas of Spain. Recently, we have assessed the overall performance of three phenomenological models for UV irradiance estimation (A, B and Erythema), using data from five sites described in Table 2 and the total ozone column from the Modern-Era Retrospective analysis for Research and Applications, Version 2 (MERRA-2) and the PM was identified as the best model for UV-E estimation (Laguarda et al, 2024) with this input information.

The main objective of this study is to complement the general results in Laguarda et al (2024) with a detailed assessment of the Power Model for UV-E, providing a breakdown of its performance under varying cloudiness conditions and solar altitudes. Particular emphasis is placed on clear sky conditions and low air mass (or high solar altitude), as these conditions are associated with high UVI levels with a potential health hazard. This new information on the PM performance will highlight its strengths and

limitations. In particular, the suitability of the PM as a tool for the long-term climatological characterization of UV-E over large regions with similar temperate climates is considered, in the context of providing reliable health advice to the population.

The paper is organized as follows. In Section 2 a description of the PM is provided. Methodological aspects and details for the data sources are provided, include the definition of sub-categories in terms of air mass and clearness index. Section 3 includes the performance indicators for each pair of sub-categories and a discussion on their significance. Finally, Section 4 summarizes our conclusions.

2 Methodology and Datasets

2.1 The Power Model (PM) approach

As mentioned in the introduction, in previous work Laguarda and Abal (2019); Laguarda et al (2024), several phenomenological models were evaluated for estimating UV-A, UV-B, and UV-E from GHI, using relative air mass (m) and total ozone column $[O_3]$ as predictors. The best performing model for UV-E, based on a product of power functions, is referred to as the Power Model (PM)

$$\text{UV-E} = a_0 \times \text{GHI} \times k_t^{a_1} \times m^{a_2} \times ([O_3]/100)^{a_3}\,, \tag{3}$$

where UV-E is in mW/m^2, GHI in W/m^2, [O$_3$] in Dobson Units (DU) and the air mas m and clearness index k_t are unitless. The air mass is computed from the solar zenith angle (or, equivalently, from the solar altitude) for a given time and location (Iqbal, 1983). The clearness index k_t is defined as the ratio of GHI to extraterrestrial irradiance projected on a horizontal plane,

$$k_t = \frac{\text{GHI}}{S_{sc} F_n \sin\alpha_s}, \tag{4}$$

where $S_{sc} = 1361$ W/m^2 is the solar constant (Kopp and Lean, 2011), F_n is the orbital (or Earth-Sun distance) correction factor (Spencer, 1971) and α_s is the solar altitude angle.

The coefficients $a_i (i = 0, 1, 2, 3)$ in Eq. (3) have been obtained in Laguarda et al (2024) adjusting data from four sites with similar temperate climates described in Table 2. The average set of coefficients from these four sites, shown in Table 1, defines an "average model" which is well suited for satellite-based estimation of UV-E over broad regions although it will be less accurate than a locally adjusted model over a given site based on local GHI measurements. For comparison, the second row in Table 1 provides the site-specific coefficients for the LES site. This approach is useful because the four sites in Table 2 share similar characteristics.

2.2 Performance Metrics

Three performance metrics frequently used in the solar resource assessment field are used to assess the performance of the UV-E model: Mean Bias Deviation (MBD), Root

Table 1 Set of coefficients for the Power Model (PM), Eq. (3), from Ref. Laguarda et al (2024).

	a_0	a_1	a_2	a_3
average model	0.705	-0.207	-1.247	-0.950
local model (LES)	0.545	-0.247	-0.942	-0.783

Mean Squared Deviation (RMSD) and Kolmogorov-Smirnov Integral (KSI) (Gueymard, 2014). The first two are defined, in terms if the residuals, $\varepsilon_i = \widehat{y_i} - y_i$, where $\hat{y}_i$ represent the modeled irradiances and y_i are the corresponding measured irradiances, as

$$\text{MBD} = \frac{1}{N}\sum_{i=1}^{N}\varepsilon_i, \tag{5}$$

$$\text{RMSD} = \left[\frac{1}{N}\sum_{i=1}^{N}\varepsilon_i^2\right]^{\frac{1}{2}} \tag{6}$$

respectively, where N is the number of samples. Both metrics (in mW/m^2) express different aspects of the accuracy of a model and are linked by the standard deviation of the residuals, σ, which quantifies the variability of the model's errors around its mean bias

$$\sigma = \sqrt{\text{RMSD}^2 - \text{MBD}^2}. \tag{7}$$

Notice that $\sigma \leq RMSD$ and an unbiased model verifies $\sigma = RMSD$. This is a useful relation for visualizing performance results in a circular diagram, as shown in Subsection 3.2.

The Kolmogorov-Smirnov Integral or KSI (Espinar et al, 2009) measures the statistical similarity between the cumulative probability function for the model's estimates and measured values ($\hat{F}$ and F respectively) across a common range for the target variable y,

$$\text{KSI} = \int |\hat{F}(y) - F(y)|\, dy. \tag{8}$$

KSI is always positive and has irradiance units, with lower values indicating greater statistical similarity between the datasets. While a low rRMSD value often corresponds to a low KSI, these two metrics capture different aspects of the model's performance.

Relative versions of these indicators, rMBD, rRMSD, σ_r and rKSI, are expressed as a % of the average $\langle y \rangle$ of the measurements, i.e. $\sigma_r = 100 \times \sigma / \langle y \rangle$.

2.3 Data for model assessment

2.3.1 Ground measurements

The dataset used in this work is a subset of the one used in Laguarda et al (2024), from which one site without UV-E measurements has been removed. Simultaneous ground GHI and UV-E measurements, taken at 1-minute intervals, from four temperate sites are used. The data was collected between 2018 and 2021 in all cases. Location details,

climate classification (Köppen-Geiger scheme Peel et al (2007)) and number of (GHI, UV-E) pairs after quality control are indicated in Table 2.

Details on instrumentation and quality control procedures are described in Laguarda et al (2024), so only a brief overview is included here for completeness. The datasets were reduced to 10-minute intervals prior to processing. This time resolution reduces short term variations and is sufficient to enable later use of the PM with GHI estimates based on geostationary satellite cloud information (GOES series), which are available with this time resolution since 2017 (Laguarda et al, 2020).

Table 2 Measurement site information and updated Köppen Geiger climate classification (Peel et al, 2007). The number of records (and % relative to records with solar altitude (α_s) greater than 7°) that passed the quality control filters (see Table 3) are shown in the last column. Coordinates are in degrees and altitude is above mean sea level in meters.

Site location	Code	Lat.	Lon.	Alt.	Climate	Records (QC %)
Salto, Uruguay	LES	-31.28	-57.92	56	Cfa	59026 (95.0)
Golden, USA	GCO	+39.74	-105.18	1829	Dfb	78901 (99.0)
Goodwin Cr., USA	GWN	+34.25	-89.87	98	Cfa	77765 (96.4)
Pilar, Argentina	PIL	-31.68	-63.87	330	Cfa/Cwa	58431 (90.0)

For the assessment of the UV-E estimates, it is desirable to exclude infrequent or atypical measurements. To this end, a quality control procedure was applied to GHI and UV-E measurements in order to filter extreme values. The filters for GHI are the lower and upper bounds recommended by the Baseline Surface Radiation Network (BSRN) (McArthur, 2005). In the case of UV-E, since typical fractions UV-E/GHI decrease with air mass and increase with solar irradiance, lower and upper bounds can be applied to them. In addition, a threshold solar altitude of $\alpha_s > 7°$ is used since hemispherical measurements, such as GHI and UV-E, are prone to high directional (cosine) errors under low-Sun conditions. These filters are briefly described in Table 3 in terms of site-dependent parameters. The bounds for the fractions are expressed as a function F, defined as $F(c, f, a; z) = c + f(\cos z)^a$, with z the solar zenith angle and $S_0 = 1361\,\mathrm{W/m^2}$ the long-term average solar irradiance (solar constant) at the top of the atmosphere (TOA). Their coefficients values and the detailed results for each filter at each site are reported in Laguarda et al (2024).

The results of the filtering procedure can be read from the last column in Table 2, where the % of the high Sun records ($\alpha_s > 7°$) that pass the filtering procedure is indicated for each site. The best data is from Golden, Colorado (a site from the

Table 3 Summary of filters applied to the data.

description	condition for valid record
solar altitude threshold	$\alpha_s > 7°$
GHI bounds (BSRN)	$c_1 \leq GHI/S_0 \leq F(c_2, f_2, a_2; z)$
UV-E fraction bounds	$F(c_1, f_1, a_1; z) \leq 10 \times \text{UV-E}/GHI \leq F(c_2, f_2, a_2; z)$

National Renewable Energy Laboratory, NREL) with 99% of high Sun records passing the filters. The worst case is from the site at Pilar, Cordoba, Argentina, with 10% of the records being discarded. As a result of this procedure, more than 274000 10-minute records from a three-year period at these sites are available for the assessment of the PM, Eq. (3).

2.3.2 Clearness index distributions

The clearness index, defined in Eq. (4), is an indicator of cloud cover and atmospheric transparency, with lower values typically associated with full cloud cover and higher values corresponding to clear-sky conditions. Fig. 2 presents the histograms of k_t for the four study sites, illustrating the distribution of clear-sky and cloudy conditions in each of them. These distributions provide insight into the predominant atmospheric conditions at each location, which must be similar in order to use an average model successfully. They also provide context for defining categories (Subsection 2.4) and for the assessment of the model's performance under different sky conditions (Section 3).

In all cases, samples corresponding to clear-sky conditions (high k_t) are grouped around a peak in the 0.70–0.85 range. The histograms for GCO and GWN are slightly bi-modal, with a secondary broad peak in the 0.10–0.30 range, associated to overcast conditions, more frequent at these sites. Except for GWN, the most probable value (at high k_t) includes more than 8% of the samples. In the case of GWN, this is below 6% of the samples, indicating that at this site cloudy conditions are indeed more frequent. Despite these small differences in cloudiness frequency, all four sites exhibit similar k_t distributions, particularly in the clear-sky range.

2.3.3 Ozone information (MERRA-2)

As mentioned in Section 1, stratospheric ozone plays an important role in the attenuation of UV-E irradiance (in particular, its UV-B component) and it must be considered as a relevant variable for UV-E estimation. In this work, the total ozone column, $[O_3]$ from MERRA-2 (Gelaro et al, 2017) is used at each site. This database provides global ozone estimates (among several meteorological variables) using the Global Earth Observing System Version-5 (GEOS-5) numerical atmospheric model. This dataset offers hourly values covering a long-term period from 1980 to the present without gaps. It has a spatial resolution of $0.5° \times 0.625°$ (latitude, longitude) or (approximately) 50×50 km cells. Although satellite-based ozone datasets, such as from Moderate Resolution Imaging Spectroradiometer (MODIS), could also be used, their lower temporal resolution (one sample per day) introduces limitations. MERRA-2 was chosen for its higher temporal resolution and continuous data availability.

The integration of several series of satellite-based ozone observations into MERRA-2's reanalysis is achieved through the GEOS-5 (Goddard Earth Observing System, Version 5) data assimilation system (Rienecker et al, 2008) which combines them with model simulations to produce consistent and accurate hourly estimates of both total column ozone and vertical ozone profiles. In recent work (Laguarda and Osorio, 2025) the ozone estimates (monthly averages) where compared to long-term Dobson measurements at two sites in the target area of this work (Salto and Buenos Aires). The results for the LES site, based on 147 months of measurements, show a small

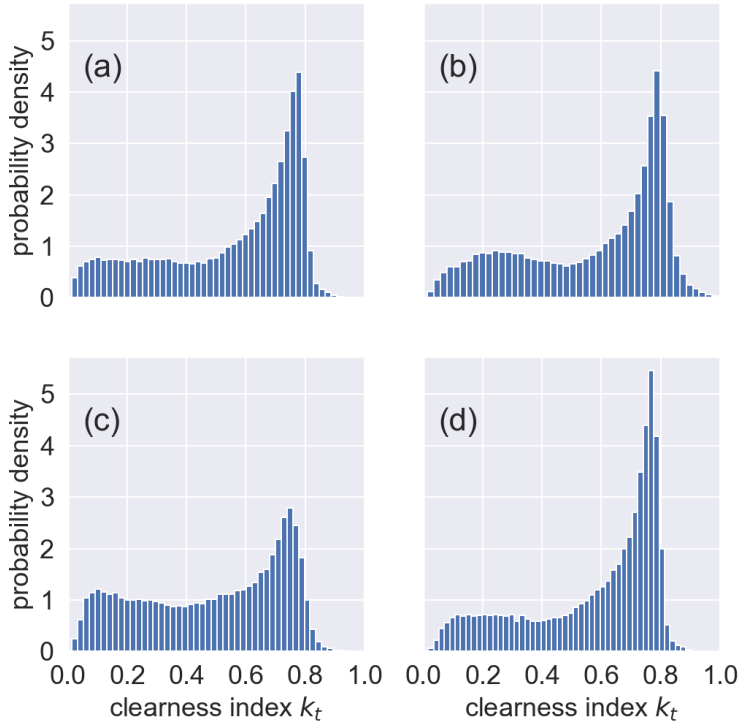

Figure 2 Probability density histograms with 50 bins for the clearness index (k_t) at each site: (a) LES, (b) GCO, (c) GWN and (d) PIL.

bias (rMBD) of 1.5% and a dispersion (rRMBD) of 2.0 % relative to the long term average of 273 DU. The average yearly cycle of $[O_3]$ shows a minimum of 260 DU at the end of summer (March in the Southern Hemisphere) and a maximum of about 300 DU in Spring (September in the Southern Hemisphere), simultaneous with the seasonal ozone depletion at higher southern latitudes, see Laguarda and Osorio (2025) for a detailed assessment of seasonal variations of the total ozone concentration over Southeastern South America.

For each site listed in Table 2, the hourly information for ozone from MERRA-2 (in DU) for the years 2018-2021 has been linearly interpolated to 10-minute intervals for its use as an input variable to the PM.

2.4 Categories for detailed analysis

The data is classified into three categories based on Sun elevation (or, equivalently, air mass), and three categories describing cloud cover conditions. Additionally, a separate

category for high irradiance conditions is considered. Performance indicators are then evaluated for each category.

Instead of using directly the solar altitude angle, α_s, the hour angle, ω, at the mid point of each 10-min data record is used to classify records into three groups: **Noon**- within 30 minutes of solar noon ($\omega = 0$), **HS**- within 90 minutes of solar noon, and **MS**- more than 90 minutes away from solar noon. Since the hour angle changes at the fixed rate of 15 °/hour, the classification criteria for proximity to Solar noon (as a proxy for Sun elevation or air mass) are listed in the first three rows of Table 4. Note that the Noon category is included in HS, and the MS category includes records with $|\omega| > 22.5°$ and $\alpha_s > 7°$, since low Sun conditions are excluded from the analysis in the quality control procedure (Table 3). Fig. 3 shows the k_t histograms for the MS and HS solar elevation categories for one site. The HS category, panel (a), includes some cloudy conditions and, conversely, the MS one, panel (b), still includes clear-sky conditions in a well defined peak at $k_t \approx 0.75$.

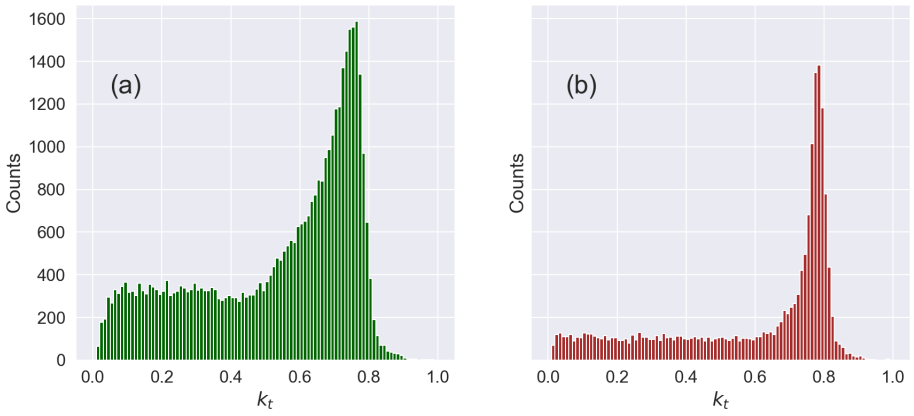

Figure 3 k_t histograms by solar elevation category for the LES site, expressed in raw counts. (a) MS category and (b) HS category.

Cloudiness is the main factor affecting solar irradiance at ground level and the clearness index k_t is a convenient indicator for cloudiness. As Fig. 2 shows, the main peak (mostly clear skies) takes place at values above $k_t > 0.70$. The selection of a threshold for completely covered skies is not so obvious, because the secondary peak is not well defined at some sites. However, values $k_t < 0.20$ are usually associated to full cloud cover. We choose these boundaries as reasonable options for these sites, keeping in mind that a slightly different choice will not affect the results significantly[2]. A k_t histogram colored by cloudiness category is shown in Fig. 4 for one site, as an

[2]We have checked this, by using (0.25 and 0.65) as k_t boundaries. This affects the numbers slightly, but not the qualitative conclusions that can be drawn from them.

Table 4 Categories used to analyze the detailed model's performance in terms of the solar hour angle (ω) and clearness index (k_t).

category	condition	characteristic
Noon	$\lvert\omega\rvert < 7.5^\circ$	within 30 min. of solar noon
High α_s (HS)	$\lvert\omega\rvert \leq 22.5^\circ$	within 90 min. of solar noon
Medium α_s (MS)	$\lvert\omega\rvert > 22.5^\circ$	more than 90 min. away from solar noon
FC	$k_t < 0.25$	mostly complete cloud cover
PC	$0.25 \leq k_t \leq 0.70$	partial cloud cover
CS	$k_t > 0.70$	mostly clear sky
HI	CS & Noon & Summer	High irradiance conditions

example. This categorization by cloudiness includes records close and away from solar noon, but separates the clear-sky peak from the other sky conditions.

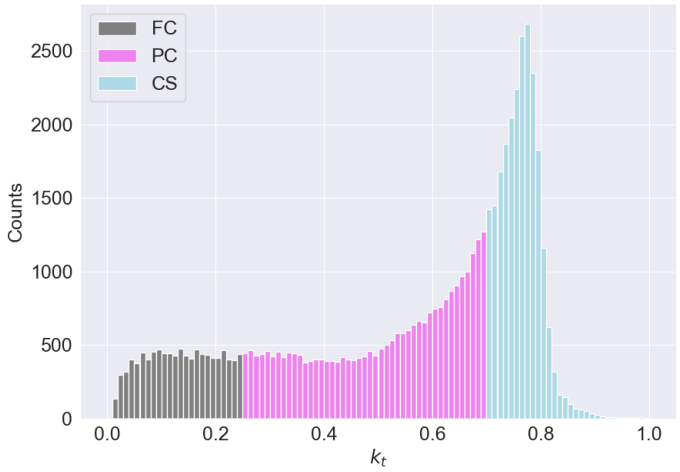

Figure 4 k_t histograms by cloudiness category for the LES site, expressed in raw counts.

As mentioned previously, the long-term objective of this work is to generate reliable statistical information on extreme values of UV-E and estimate the dosage for different exposure times within the context of its impact on human health. In particular, the suitability of the PM to be used with satellite-based GHI estimates (Laguarda et al, 2020) with high accuracy and large spatial coverage to generate maps of UV-E with expected maximal dosage over the target territory is of interest. For these application, the performance of the UV-E model under maximum irradiance conditions is particularly relevant. Thus, an additional category for High Irradiance conditions (HI) is defined as follows:

- Summer months (in a broad sense): December to March for LES and PIL sites and June to September for GCO and GWN sites.
- Noon records (i.e. those within 30 min of solar noon).
- Clear sky records in the CS category ($k_t > 0.70$).

as described in compact form in the last row of Table 4. In order to provide further insight into these categories, the averages and standard deviations of selected variables are provided in in Table A1 and Table A2 for the LES site. These categories will prove to be useful to analyze the performance of UV-E estimates from Eq. (3).

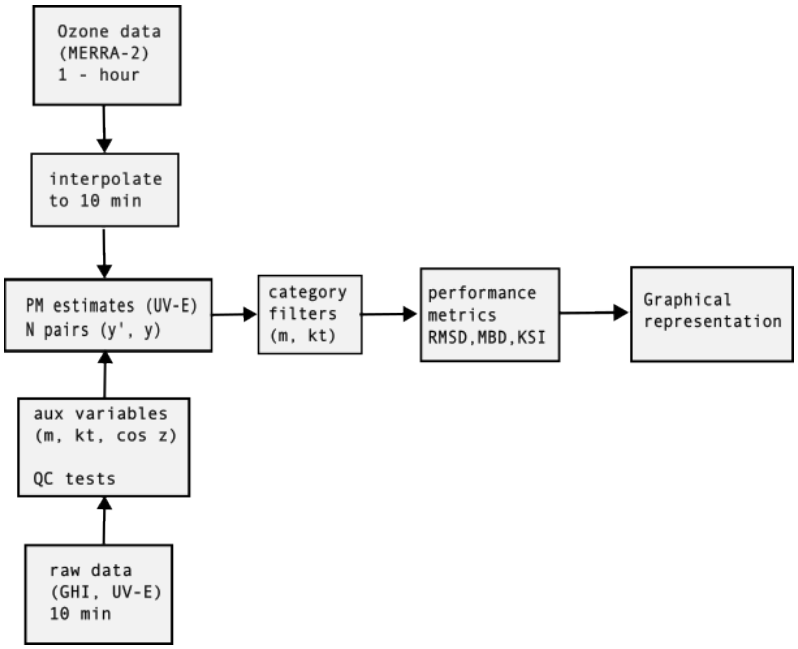

Figure 5 Simplified flowchart describing the methodology applied at each site.

The methodology described in this Section is outlined in the flowchart diagram presented in Fig. 5. For each site, raw data at 1-min intervals for solar irradiance (GHI, UV-E) are averaged to 10-min intervals, auxiliary variables such as air mass, solar altitude angle and clearness index are calculated and quality control filters are applied. Total Ozone information from MERRA-2 at 1 hour time steps is linearly interpolated to 10-min intervals. Data at 10-min intervals is used to evaluate the PM estimates and N pairs $(\hat{y}, y$ corresponding to the measured UV-E and its PM estimate are formed. These pairs are categorized according to clearness index and solar altitude (in the particular case of the HI category, the day of year is also relevant). Performance metrics are calculated for each subcategory pair and a graphical representation is displayed.

3 Results and Discussion

In this section, the performance analysis results for the PM are presented. Since the average irradiance varies significantly across the different categories representing solar altitude and cloud conditions (see Table A1 and Table A2), absolute metrics such as MBD and RMSD, while useful for inter-site comparisons, are not suitable for comparisons between different categories at the same site. Thus, to facilitate meaningful comparisons between categories, relative metrics (expressed as percentages of the mean measurements for the category) are also used. This dual approach allows for a clearer assessment of model performance across different sites and varying atmospheric conditions.

3.1 General Performance Overview

The overall performance indicators for the average PM, Eq. (3), at the four sites listed in Table 2 were previously evaluated (Laguarda et al, 2024) and are summarized in Table 5, as they provide the context for the more detailed analysis presented below.

Table 5 Performance indicators (absolute and relative) for UV-E estimates from Eq. (3) with MERRA-2 ozone inputs and average coeficients, adapted from Ref. Laguarda et al (2024). The last row shows the average of the measurements used as a reference for the relative values. The last column shows the mean values across sites.

	LES		**GWN**		**GCO**		**PIL**		**Mean**	
	mW/m^2	%	mW/m^2	%	mW/m^2	%	mW/m^2	%	mW/m^2	%
MBD	-2.7	-3.0	-1.3	-1.9	3.8	5.4	3.0	3.5	8.5	1.1
RMSD	9.1	10.3	8.0	11.8	7.9	11.3	7.4	8.8	8.3	10.7
KSI	5.9	6.7	4.1	6.0	1.6	2.3	3.7	4.4	3.7	4.7
<UV-E>	88.6		67.7		69.8		84.3		77.7	

The MBD ranges from $-3\,mW/m^2$ (under-estimation) to $4\,mW/m^2$ (over-estimation) and the RMSD remains below 10 mW/m^2, indicating reasonable accuracy. As a reference, the typical uncertainty is below 12%. These are good performance indicators, considering that the corresponding uncertainty for a good field GHI ground measurement is about 5% of the average. As expected, these UV-E estimates derived from local measurements and locally adjusted models are more accurate than the global satellite-based estimates from RTM calculations discussed in Subsection 1.1.

These indicators provide a general performance overview but they can also be misleading. For example, a scatter plot of the estimated UV-E irradiance vs. measurements for the LES site (Fig. 6(a)) shows that the model overestimates UV-E at high irradiances, yet the overall bias is negative (-3.0%), indicating that there are negative biases at other conditions which overcome the positive bias at high UV-E. The opposite occurs with GCO, with an underestimation for high UV-E values evident in Fig. 6(b) with an overall rMBD of +5.4% indicating the predominance of overestimation. Since high UV-E conditions can result from either clear skies or high Sun elevations under

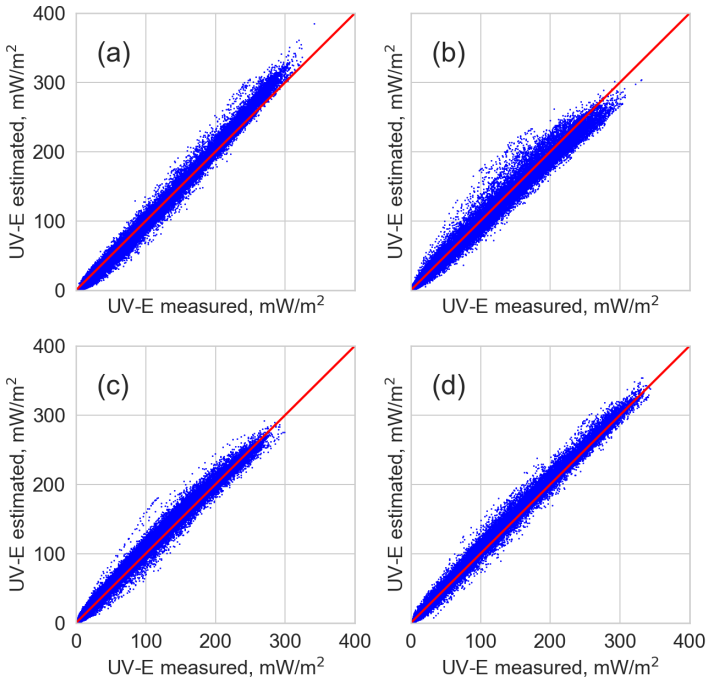

Figure 6 Scatter plots for estimated UV-E from Eq. (3) vs measured for each site: (a) LES; (b) GCO; (c) GWN and (d) PIL. The same average model was used for all sites. The red line corresponds to a perfect match.

partial cloudiness, it is crucial to analyze the model's behavior across different atmospheric conditions. Understanding how specific factors contribute to dispersion and bias will provide insight into its suitability for long-term regional applications.

3.2 Performance breakdown with solar altitude or cloudiness

When the data is categorized by solar altitude or cloudiness, the corresponding MBD and RMSD results are shown in Fig. 7. The blue bars represent the uncategorized data, shown as a reference.

The average model considered here is based on a unique set of coefficients and is therefore not unbiased. The model shows overall overestimation (positive bias) at GWN an PIL and underestimation (negative bias) at LES and GCO. Absolute biases are consistently larger across sites under Noon or HS conditions. Two sites (GWN, PIL) show high positive biases under clear skies (CS), but the other two have either small negative or negligible bias under the same conditions, so general conclusions cannot be drawn.

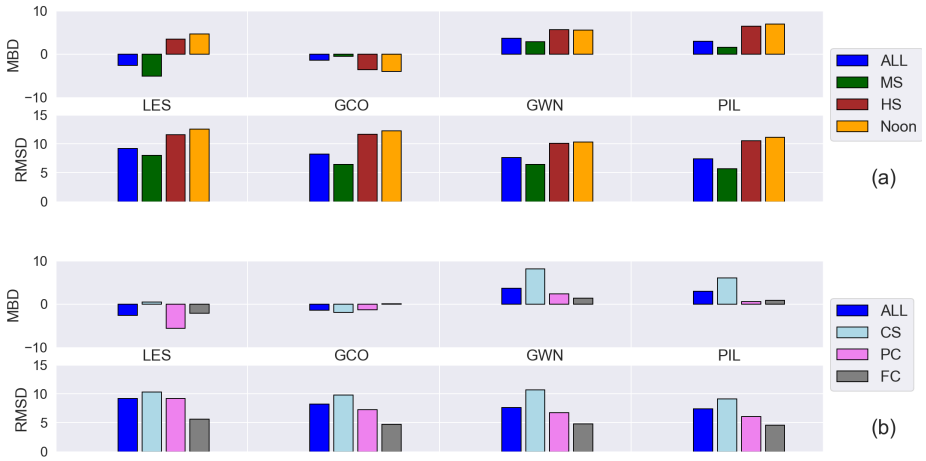

Figure 7 Absolute performance indicators, in mW/m^2, for categorized data. (a) Solar altitude categories and (b) Cloudiness categories.

Overall, dispersion, as measured by the RMSD, is greater under Noon and clear-sky conditions. However, this increased dispersion is only seen with absolute performance metrics since the average UV-E is higher in these categories, which contributes to larger dispersion values. Table A4 includes the same performance indicators in relative terms and in that case, rRMSD is lowest for the HS and Noon categories across sites.

To explore this matter further, the relative metrics (expressed as percentages of the mean measurements for each category) in Table A4 are presented as circular diagrams (Taylor, 2001) in Figs. 8 and 9, offering a more comprehensive visualization. All the performance indicators are expressed in relative terms as a percentage of the mean UV-E irradiance measurement for each category (listed in the last row of Tables A1 to A3). These diagrams show the standard deviations of the residuals (σ_r) vs. the rMBD and the distance of each point to the origin is rRMSD $= \sqrt{\text{rMBD}^2 + \sigma_r^2}$, according to Eq. (7). The origin (0,0) represents a perfect agreement between model and measurements and an unbiased model would be on the vertical axis.

In these diagrams, each site is represented by a geometric symbol and the different categories are represented by the usual color code (the ALL category is included in blue as a reference for overall performance). Fig. 8 presents the relative metrics for solar height categories. For MS conditions, biases exhibit variable signs, ranging from -7.7% (LES) to +6.0% (GWN), while the variability (as represented by σ_r) spans from 9,1% (PIL) to 12.9% (GCO). As solar elevation increases, the behavior changes. Under HS conditions, biases tend to be positive and remain below 4.8%, except for GCO, which shows a negative bias of -2.9%. Meanwhile, dispersion decreases to values between 5.7% (PIL) and 9.2% (GCO). Specifically at Noon, biases are similar to those observed under HS conditions, while dispersions are slightly lower, ranging from 5.6% to 9.0%.

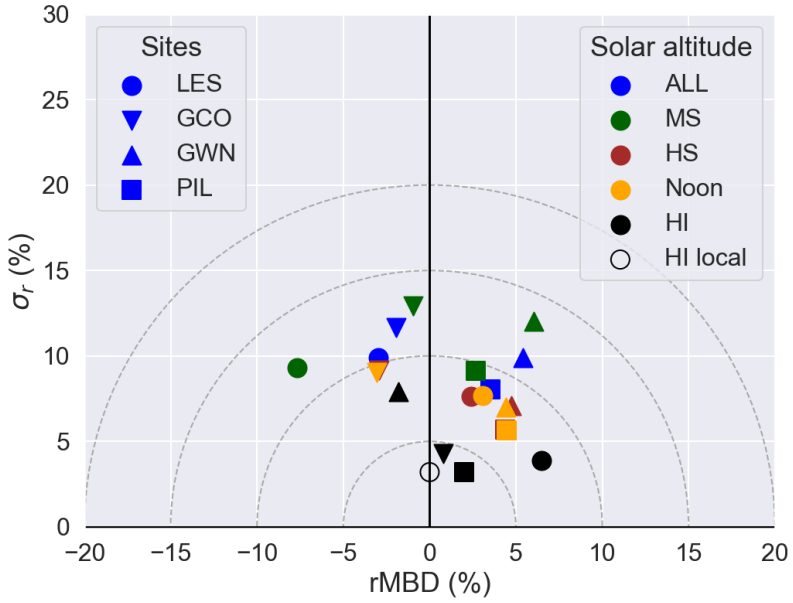

Figure 8 Circular diagrams showing the relative standard deviation of the residuals vs. rMBD for each solar altitude category and site. The dashed circles represent the rRMSD at 5% intervals.The High Irradiance category (HI) (Subsection 3.4) is also included (black symbols) for the LES site as filled (average PM) or unfilled (local PM) circles.

In Fig. 9 the corresponding results are shown according to cloudiness conditions. Under overcast conditions (FC), biases range from -8.8% (LES) to +7.7% (GWN), while relative dispersions are high, reaching 28.0% at GWN. For the partially cloudy (PC) category, absolute biases decrease, ranging between -9.0% and +4.2%, while dispersion also decreases, with values between 11.6% and 15.8% (GCO). Finally, under clear sky (CS), relative biases range from -1.7% (GCO) to +6.1% (GWN) and dispersions are the smallest, in the range of 5.0% to 9.0%. Overall, the relative dispersion tends to decrease as solar height increases (Fig. 8) or cloudiness decreases (Fig. 9).

These results are presented in detailed form in Table A4. They complement the findings presented in Fig. 7 in terms of absolute metrics. There, it is evident that under high irradiance conditions (whether due to clear skies or high solar elevation) the absolute metrics tend to increase. However, they increase at a lower rate than the average irradiance, resulting in lower relative metrics for these categories, as discussed.

3.3 Two-dimensional analysis

The relative performance indicators obtained by simultaneously varying Sun elevation and cloudiness categories are presented for each site in Table A4. For this graphical representation, the solar altitude angle and the clearness index are subdivided into 10 bins each, generating 10×10 matrices for each performance indicator. Fig. 10 displays

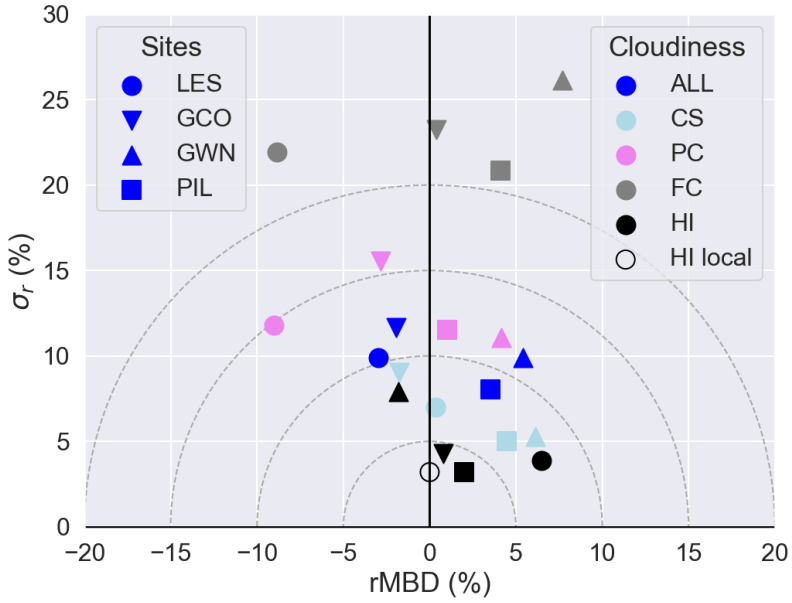

Figure 9 Circular diagrams showing the relative standard deviation of the residuals vs. rMBD for each cloudiness category and site. The dashed circles represent the rRMSD at 5% intervals. The High Irradiance category (HI) (Subsection 3.4) is also included (black symbols) for the LES site as filled (average PM) or unfilled (local PM) circles.

the rMBD and rRMSD matrices for two representative sites, LES and GCO. Each metric in a given bin is expressed as a percentage of the corresponding measurements average, which is shown in the rightmost column of Fig. 10.

This figure highlights distinct performance patterns associated with sky conditions (k_t) and the sine of the solar altitude angle. The plots in the rightmost column depict an expected trend, showing that the average UV-E irradiance increases with higher solar altitude (high $\sin \alpha_s$) and clearer sky conditions (high k_t).

As the first column shows, the rMBD is low under high Sun conditions except for full cloud cover. The second column shows the rRMSD indicator (dark blue is lowest). For high Sun conditions and particularly under clear skies, this indicator is lowest. Thus, the model represents UV-E irradiance most reliably under clear-sky conditions.

In contrast, under cloudy conditions, the model exhibits the larger biases (with signs that are site-dependent) and the largest dispersions, reflecting the inherent challenges of accurately modeling UV-E when clouds introduce variability through a complex attenuation of the incident solar irradiance. This is observed across all solar altitudes. At solar noon, particularly under partially cloudy skies, the model shows medium to high dispersions. This increased variability can be attributed to rapid changes in cloud cover coupled with high solar altitudes, which impact the accuracy of the global irradiance estimates.

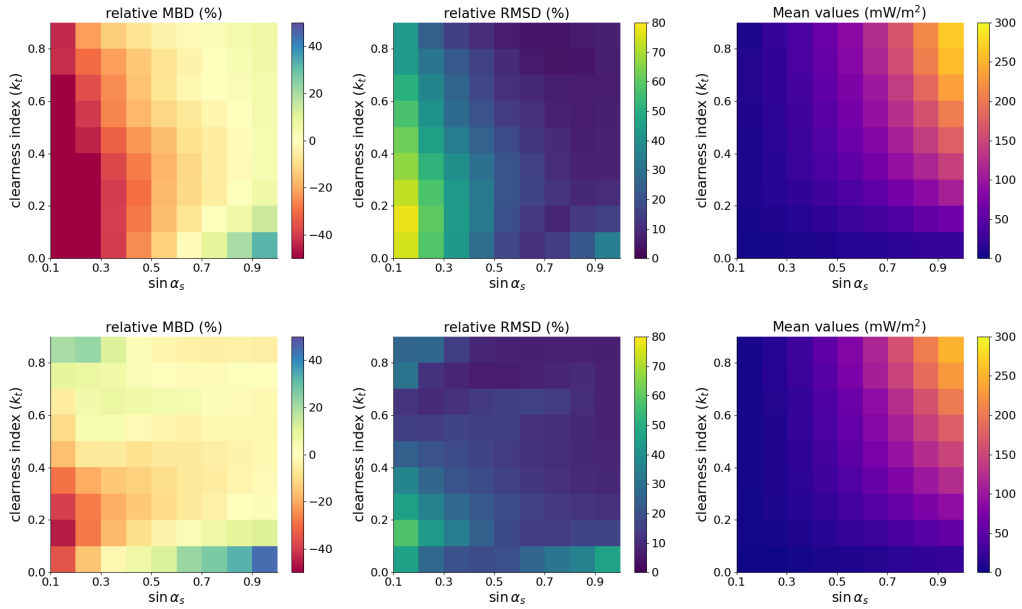

Figure 10 Breakdown of performance indicators (rMBD and rRMSD expressed in %) in 10×10 bins of $\sin(\alpha_s)$ and clearness index. The panels in the last column indicate the measurements average in each bin, used to calculate relative metrics of the first two columns. The first row corresponds to the LES site and the second to GCO.

This analysis suggests that the PM is capable of estimating UV-E with good accuracy, particularly under clear sky conditions, and highlights its limitations under partial or full cloud cover, especially close to solar noon.

3.4 High Irradiance conditions (HI)

The number of records per site and the average values of selected variables within the High Irradiance conditions (HI) category, defined in Subsection 2.4, are shown in Table A3, together with the average values of relevant variables and their standard deviations. The corresponding performance indicators for this HI category are shown in Table 6.

The relative mean bias deviation (rMBD) has site-specific values ranging from a +6.5% overestimation at LES to a -1.8% (underestimation) at GWN. This variability represents an obstacle when applying the average model coefficients to different locations and highlights the impact of local atmospheric characteristics on the accuracy, even under clear skies and at solar noon. The model performs consistently well at GCO and PIL, with smaller biases indicating reliable maximum UV-E estimates during high UV irradiance in summer.

Relative root mean square deviation values show low overall dispersions, averaging 5.9% of the average of the measurements. LES and GWN have higher (but still acceptable) rRMSD values around 8% while GCO and PIL exhibit lower dispersions around 4%, indicating a very good agreement. The relative KSI, which averages 3.1%

Table 6 Relative performance indicators data the HI category, expressed as % of the average of the corresponding UV-E measurements (listed in Table A3). The first column corresponds to the locally adjusted (unbiased) model for the LES site (coefficients from the second row of Table 1). The last column shows the average performance indicators of the average model across sites as a % of the overall UV-E average, 246.9 mW/m^2.

metric	LES (local)	LES	GWN	GCO	PIL	average
rMBD (%)	0.0	6.5	-1.8	0.8	2.0	2.4
rRMSD (%)	3.2	7.6	8.1	4.4	3.8	5.9
σ_r (%)	3.2	3.9	7.9	4.3	3.2	5.4
rKSI (%)	0.4	6.4	2.1	1.7	2.0	3.1

across sites, also indicates a good statistical similarity between the PM estimates and measurements. The performance indicators for the HI category have been included in the circular diagrams, Figs. 8 and 9 (black symbols) to show them in the context of the other categories. It is easily visualized that the HI conditions (clear sky, high Sun and summer) lead to the PM best performance.

Non-negligible mean biases are to be expected from an average model, but they represent a particular challenge for the characterization of UV-E over climatological time scales, since they are not reduced by averaging or aggregation of the data. This can be solved by adjusting the coefficients to each site to obtain an unbiased version of the PM. The first column in Table 6 shows the performance indicators for the local (unbiased) PM at LES, in order to analyze the effect using a locally adjusted model. Fig. 11 shows the scatter plots for the average and unbiased versions of PM at the LES site which visually show the effect of local adjustment. The performance of the local model for the LES site is also shown in the circular diagrams, Figs. 8 and 9, as an unfilled black circle which shows the model is unbiased and has the smallest σ_r and rRMSD.

These findings confirm the model's strong performance under clear, high-sun conditions, while highlighting areas for refinement to enhance consistency and reduce variability for broader applicability. The performance of the unbiased model is impressive (second column of the Table 6), considering that the typical error in a field UV-E measurement is between 5 and 10% of the average of a set of measurements, depending on the quality and maintenance schedule of the instrument.

4 Conclusions

The use of a power model for estimating erythemal UV irradiance from global horizontal irradiance, relative air mass, and ozone column data is assessed under different atmospheric conditions. Total atmospheric ozone estimates from a reanalysis database (MERRA-2) where used. These results complement previous work in which the empirical coefficients of PM were determined using data from four mid-latitude temperate sites in North and South America and its overall accuracy was analyzed. This first assessment showed low biases (rMBD) ranging from -3.0% to +5.4% and dispersions (rRMSD) below 12%, in both cases relative to the mean of the measurements. Building on that work, this study extends the performance assessment by evaluating the

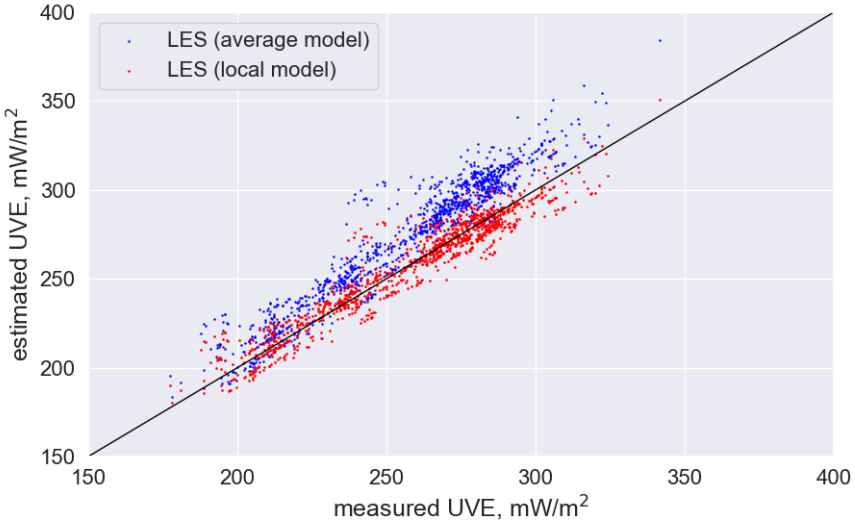

Figure 11 Scatter plot for UV-E records in the HI category at the LES site (1178 data records). In blue, the average PM, and in red, the unbiased (local) model. The corresponding performance indicators are listed in the first two columns of Table 6.

average model (i.e. a single set of average coefficients is used at all sites) performance under different solar altitudes, cloudiness conditions and Ozone concentrations, offering detailed insights into its strengths and limitations under diverse atmospheric scenarios.

The analysis of the model's performance across solar time shows a good agreement with the measurements under high solar altitudes and near-noon conditions, with mean biases between -3 % and +5 % and dispersions between 6 % and 9 %. At medium solar altitudes, biases vary more (from -7.7% to +6.0%) and dispersions are larger (9-13%). These results show the model's accuracy under high-sun conditions, most important for exposure risk assessments, while highlighting its limitations under lower solar altitudes.

Regarding cloud conditions, as indicated by the clearness index, the model has better accuracy under clear skies, with biases ranging from -2% to +6% and dispersions in the 5-9 % range. For partially cloudy conditions, biases remain moderate (-9 % to +4 %), but dispersions increase at some sites. The performance decreases under overcast conditions, where biases become larger (-9 % to +8 %) and dispersions exceed 20%. Part of this is an artifact of expressing relative indicators relative to the measurement average, which is lower under cloudy skies. However, there are challenges for accurate modeling UV-E under variable or high cloud cover conditions, since ground albedo, multiple reflections and other complex attenuation effects are only partially accounted for by the current parametrization.

High irradiance conditions where particularly investigated due to their relevance for parameters such as maximum daily UV index or daily UV-E doses, which are of interest for health-related applications. High irradiance conditions (HI) are defined here as

solar noon under clear skies during summer months (i.e. the highest solar altitudes). Within this category, the model performs best, showing a strong agreement between estimates and measurements with an average rMBD of 2.4% and rRMSD of 5.9% averaged accross sites. Site-specific analyses reveal local variations, such as a higher positive bias at one site (LES, +6.5%) and a slight underestimation at another (GWN, -1.8%). These discrepancies highlight the impact of local atmospheric characteristics on the model accuracy, due to the use of a single set of coefficients at all sites. Regarding dispersion, it was higher at LES and GWN compared to GCO and PIL, where the model performed more accurately. The relative KSI supports these findings, showing a good statistical agreement between measured and modeled UV-E distributions.

As a test of maximum potential accuracy, an unbiased version of the model (i.e. with locally adjusted coefficients) showed an rRMSD of only 3.2% under HI conditions, which is similar than the typical error associated to field UV instruments. In view of these results, when the model is applied to calculate long-term (several years) doses or cumulative values, it is strongly recommended to employ an unbiased version with locally adapted empirical parameters.

These findings represent a firm basis for the generation of reliable UV-E datasets for long-term climatological analyses, including extreme UV-E values and cumulative daily dose estimations. Very good accuracy can be obtained at specific sites for which a set of (GHI, UV-E) measurements are available using an unbiased version of the model. The average version of the model, when used with satellite-derived GHI and ozone column from global databases, can provide good UV-E estimates over broad geographical regions.

Appendix A Auxiliary information

The data was categorized into either solar altitude (MS, HS and Noon) or clearness index (FC, PC, CS) categories, as defined in Table 4. To provide context, the Table A1 lists the average and standard deviations of selected variables within each solar elevation category for LES site, while Table A2 presents the same variables for cloudiness categories. The standard deviations give an indication of the spread of each variable within its respective category.

Although the average clearness index remains nearly constant across solar elevation categories, the average UV-E varies significantly. In contrast, cloudiness categories exhibit visible differences in average k_t values. The first column of Table A1, which corresponds to the uncategorized datasets, is repeated in Table A2 for clarity. Similar patterns are observed at the other sites. The average of the UV-E measurements can be very different between categories or between sites.

When the performance of the model from Eq. (3) is evaluated varying both the solar altitude and cloudiness categories, 4×4 matrices of performance indicators are obtained for each site for each metric. The rMBD and rMBD are shown together with the standard deviation of the residuals, σ_r, calculated from Eq. (7). A graphical representation of this information is shown (in absolute terms) in Fig. 10 for the LES

Table A1 Average and standard deviations of selected variables in the solar elevation categories for the LES site. Refer to Table 4 for category definitions.

solar elevation cat. →	**All**	**Noon**	**HS**	**MS**
abs. hour angle, $\|\omega\|$ (°)	40.3 ± 24.2	3.8 ± 2.2	11.2 ± 6.5	52.0 ± 18.2
solar altitude, α_s (°)	37.4 ± 18.5	56.5 ± 16.3	54.2 ± 15.4	30.7 ± 15.0
relative air mass, m	2.2 ± 1.4	1.3 ± 0.3	1.3 ± 0.3	2.6 ± 1.5
clearness index, k_t	0.6 ± 0.2	0.6 ± 0.2	0.6 ± 0.2	0.5 ± 0.2
meas. UV-E, mW/m^2	88.6 ± 75.7	151.6 ± 84.7	144.8 ± 82.4	66.2 ± 59.5
# records	59026	5623	16842	42184

Table A2 Average and standard deviations of selected variables in the cloudiness categories for the LES site. Refer to Table 4 for category definitions.

cloudiness cat. →	**All**	**CS**	**PC**	**FC**
abs. hour angle, $\|\omega\|$ (°)	40.3 ± 24.2	29.7 ± 18.5	49.1 ± 25.1	41.8 ± 24.0
solar altitude, α_s (°)	37.4 ± 18.5	46.6 ± 15.3	30.6 ± 17.8	33.7 ± 17.8
relative air mass, m	2.2 ± 1.4	1.5 ± 0.5	2.7 ± 1.6	2.4 ± 1.5
clearness index, k_t	0.6 ± 0.2	0.8 ± 0.0[1]	0.5 ± 0.1	0.1 ± 0.1
meas. UV-E, mW/m^2	88.6 ± 75.7	146.9 ± 71.5	61.7 ± 54.5	23.8 ± 20.7
# records	59026	23008	26198	9820

[1]The standard deviation of clear-sky k_t is 0.04.

Table A3 Average and standard deviations of selected variables for the High Irradiance (HI) category at each site.

	LES	**GCO**	**GWN**	**PIL**
solar altitude (°)	71.1 ± 8.4	63.3 ± 8.4	68.9 ± 8.4	73.8 ± 8.0
air mass	1.07 ± 0.06	1.14 ± 0.09	1.09 ± 0.07	1.05 ± 0.06
clearness index	0.79 ± 0.03	0.80 ± 0.04	0.77 ± 0.04	0.78 ± 0.03
UV-E (mW/m^2)	258.0 ± 30.0	223.5 ± 37.6	226.8 ± 30.5	279.4 ± 35.4
# records	1178	1670	1230	997

and GCO sites using finer 10×10 cells instead of 4×4. The relative performance indicators obtained when varying one category at a time are shown in Figs. 8 and 9.

Table A4 Relative performance indicators per category pairs as % of the corresponding mean of the measurements (see Table A5).

Site	Cloudiness	rMBD				rRMSD				σ_r			
		ALL	**MS**	**HS**	**Noon**	**ALL**	**MS**	**HS**	**Noon**	**ALL**	**MS**	**HS**	**Noon**
LES	**ALL**	-3.0	-7.7	2.4	3.1	10.3	12.1	8.0	8.3	9.9	9.3	7.6	7.7
	CS	0.3	-2.7	3.3	3.9	7.0	6.8	6.9	7.2	7.0	6.2	6.1	6.1
	PC	-9.0	-14.9	0.0	0.8	14.9	18.5	9.1	9.2	11.8	10.9	9.1	9.1
	FC	-8.8	-17.1	3.6	4.0	23.7	28.1	16.9	17.4	21.9	22.3	16.5	16.9
GCO	**ALL**	-1.9	-0.9	-2.9	-3.1	11.8	13.0	9.6	9.6	11.7	12.9	9.2	9.0
	CS	-1.7	-0.4	-3.0	-3.2	9.2	9.2	8.6	8.6	9.0	9.2	8.1	8.0
	PC	-2.8	-1.9	-4.1	-4.2	15.8	18.3	11.2	11.0	15.6	18.2	10.4	10.2
	FC	0.4	-3.1	5.6	6.6	23.3	25.7	17.7	17.7	23.3	25.5	16.8	16.4
GWN	**ALL**	5.4	6.0	4.8	4.4	11.3	13.5	8.5	8.3	9.9	12.0	7.1	7.0
	CS	6.1	8.1	4.7	4.2	8.1	9.5	7.0	6.7	5.3	5.0	5.2	5.3
	PC	4.2	4.7	3.4	3.3	11.8	13.2	8.7	8.5	11.1	12.4	8.0	7.9
	FC	7.7	2.8	14.4	15.2	27.3	28.2	23.2	23.6	26.2	28.0	18.2	18.0
PIL	**ALL**	3.5	2.7	4.4	4.5	8.8	9.5	7.2	7.2	8.0	9.1	5.7	5.6
	CS	4.5	4.5	4.4	4.4	6.7	6.8	6.3	6.4	5.0	5.1	4.6	4.6
	PC	1.0	-0.4	3.4	3.8	11.6	12.4	8.6	8.7	11.5	12.4	7.9	7.8
	FC	4.1	-0.7	10.8	11.2	21.3	21.0	18.3	18.2	20.9	21.0	14.7	14.4

Table A5 Reference mean of UV-E and number of data pairs per category pairs per site.

Site		Reference Mean (mW/m^2)				# of data pairs			
	ALL	**MS**	**HS**	**Noon**	**ALL**	**MS**	**HS**	**Noon**	
LES	**ALL**	88.6	66.2	144.8	151.6	59026	42184	16842	5623
	CS	146.9	120.5	186.8	194.1	23008	13868	9140	3076
	PC	61.7	46.5	124.0	129.9	26198	21050	5148	1721
	FC	23.8	19.3	36.5	38.7	9820	7266	2554	826
GCO	**ALL**	69.8	49.5	121.1	127.8	78901	56504	22397	7466
	CS	106.8	82.1	147.3	155.3	35907	22302	13605	4598
	PC	46.1	33.2	96.9	100.3	31073	24773	6300	2067
	FC	20.3	15.4	38.7	40.9	11921	9429	2492	801
GWN	**ALL**	67.8	47.6	117.9	124.6	77765	55486	22279	7435
	CS	132.4	107.8	158.9	167.5	20665	10737	9928	3320
	PC	56.7	41.8	115.5	122.2	39021	31102	7919	2647
	FC	17.7	13.5	30.4	31.9	18079	13647	4432	1468
PIL	**ALL**	84.3	59.7	146.0	154.1	58431	41769	16662	5566
	CS	136.5	108.4	174.9	183.0	25151	14539	10612	3581
	PC	52.2	38.8	118.5	126.0	25295	21041	4254	1415
	FC	21.6	16.2	40.3	42.2	7985	6189	1796	570

References

Antón M, Serrano A, Cancillo ML, et al (2008) Relationship between erythemal irradiance and total solar irradiance in south-western spain. Journal of Geophysical Research: Atmospheres 113(D14). https://doi.org/https://doi.org/10.1029/2007JD009627, URL https://agupubs.onlinelibrary.wiley.com/doi/abs/10.1029/2007JD009627, https://agupubs.onlinelibrary.wiley.com/doi/pdf/10.1029/2007JD009627

Antón M, A S, Cancillo M, et al (2009) An empirical model to estimate ultraviolet erythemal transmissivity. Annales Geophysicae 27:1387–1398. https://doi.org/10.5194/angeo-27-1387-2009

Antón Martínez M (2007) Modelos empíricos para la estimación de la irradiancia solar ultravioleta. PhD thesis, Universidad de Extremadura, España, URL http://hdl.handle.net/10662/496, phD Thesis

Arola A, Kalliskota S, Outer P, et al (2002) Assessment of four methods to estimate surface uv radiation using satellite data by comparison with ground measurements from four stations in europe. Journal of Geophysical Research 107:1–11. https://doi.org/10.1029/2001JD000462

Bernhard G, Bais A, Aucamp P, et al (2023) Stratospheric ozone, uv radiation, and climate interactions. Photochemical and Photobiological Sciences pp s43630–023–00371. URL https://doi.org/10.1007/s43630-023-00371-y

Copernicus Atmosphere Monitoring Service (CAMS) (2024) UV Index Product. URL https://atmosphere.copernicus.eu/charts/packages/cams-additional/products/uv-index, accessed: November 2024

Dieste-Velasco M, García-Rodríguez S, Garcia Rodriguez A, et al (2023) Modeling horizontal ultraviolet irradiance for all sky conditions by using artificial neural networks and regression models. Applied Sciences 13:1473. https://doi.org/10.3390/app13031473

Eskes H, Tsikerdekis A, Ades M, et al (2024) Technical note: Evaluation of the copernicus atmosphere monitoring service cy48r1 upgrade of june 2023. Atmospheric Chemistry and Physics pp 9475–9514. https://doi.org/10.5194/egusphere-2023-3129, URL https://acp.copernicus.org/articles/24/9475/2024/acp-24-9475-2024.pdf

Espinar B, Ramírez L, Drews A, et al (2009) Analysis of different comparison parameters applied to solar radiation data from satellite and german radiometric stations. Solar Energy 83:118–125

Gelaro R, McCarty W, Suárez M, et al (2017) The Modern-Era RetrospectiveAnalysis for Research and Applications, Version 2 (MERRA-2). Journal of Climate 30:5419–5454. https://doi.org/https://doi.org/10.1175/JCLI-D-16-0758.1

Gueymard C (2019) The smarts spectral irradiance model after 25 years: New developments and validation of reference spectra. Solar Energy 187:233–253. https://doi.org/10.1016/j.solener.2019.05.048

Gueymard CA (2004) The sun's total and spectral irradiance for solar energy applications and solar radiation models. Solar Energy 76(4):423–453

Gueymard CA (2014) A review of validation methodologies and statistical performance indicators for modeled solar radiation data: Towards a better bankability of solar projects. Renewable and Sustainable Energy Reviews 39:1024–1034

Habte AM, Sengupta M (2020) Modeling of ultraviolet irradiance from total irradiance: a simplified approach. Tech. rep., National Renewable Energy Laboratory (NREL), URL https://www.nrel.gov/docs/fy20osti/76173.pdf

Iqbal M (1983) An introduction to solar radiation. Academic Press

ISO (1999) ISO 17166:1999 and CIE-S007 Joint ISO - CIE Standard: Erythema Reference Action Spectrum and Standard Erythema dose. Electronic publication, International Standardization Organization and Commission Internationale de l'Eclairage

ISO (2007) ISO 21348:2007 Space environment (natural and artificial): Process for determining solar irradiances. Electronic publication ISO 21348:2007, International Standardization for Organization, URL https://www.iso.org/standard/39911.html

Ji Y, Cai L, Zheng T, et al (2015) The mechanism of UVB irradiation induced-apoptosis in cataract. Molecular and Cellular Biochemestry 401:87–95. https://doi.org/https://doi.org/10.1007/s11010-014-2294-x

Kopp G, Lean J (2011) A new, lower value of total solar irradiance: Evidence and climate significance. GEOPHYSICAL RESEARCH LETTERS 38:L01706

Laguarda A, Abal G (2019) Performance of simple empirical models for UV-A, UV-B and UV-E irradiance from global horizontal irradiance. In: Proceedings of the ISES Solar World Congress 2019, Santiago de Chile, Chile, Resource Assessment and Energy Meteorology

Laguarda A, Osorio M (2025) Total ozone content in southeastern south america: A statistical analysis of 45 years of satellite data. Journal of Atmospheric and Solar-Terrestrial Physics 269:106468. https://doi.org/https://doi.org/10.1016/j.jastp.2025.106468, URL https://www.sciencedirect.com/science/article/pii/S1364682625000525

Laguarda A, Giacosa G, Alonso-Suárez R, et al (2020) Performance of the site-adapted cams database and locally adjusted cloud index models for estimating global solar horizontal irradiation over the pampa húmeda. Solar Energy 199:295–307.

https://doi.org/https://doi.org/10.1016/j.solener.2020.02.005, URL https://www.sciencedirect.com/science/article/pii/S0038092X20301031

Laguarda A, Abal G, Russo P, et al (2024) Estimating UV-B, UV-Erithemic, and UV-A irradiances from Global Horizontal Irradiance and MERRA-2 Ozone column information. Journal of Solar Energy Engineering 147(2):021001. https://doi.org/10.1115/1.4066202, URL https://doi.org/10.1115/1.4066202, https://asmedigitalcollection.asme.org/solarenergyengineering/article-pdf/147/2/021001/7374598/sol_147_2_021001.pdf

Liu-Smith F, Jia J, Zheng Y (2017) UV-Induced Molecular Signaling Differences in Melanoma and Non-melanoma Skin Cancer. Advances in experimental medicine and biology 996:27–40. https://doi.org/https://doi.org/10.1007/978-3-319-56017-5

McArthur L (2005) Baseline surface radiation network operations manual. Tech. Rep. WCRP-121/ WMO TD-No. 1274, WORLD CLIMATE RESEARCH PROGRAMME - WMO

Peel MC, Finlayson BL, Mcmahon TA (2007) Updated world map of the Köppen-Geiger climate classification. Hydrology and Earth System Sciences Discussions 11:1633–1644

Pitkänen M, Wandji W, Arola A (2020) Validation report of the cams uv processor. Tech. Rep. 19, Copernicus Atmosphere Monitoring Service, URL https://atmosphere.copernicus.eu/sites/default/files/2020-11/19_CAMS72_2018SC2_D72.2.1.1-2020Q3_UV_VAL_202009_v1.pdf

Rienecker M, Suarez M, Todling R, et al (2008) The GEOS-5 data assimilation system: Documentation of versions 5.0.1, 5.1.0, and 5.2.0. Technical Report Series on Global Modeling and Data Assimilation NASA/TM–2008–104606, NASA, URL https://gmao.gsfc.nasa.gov/pubs/docs/Rienecker369.pdf

Spencer JW (1971) Fourier series representation of the position of the sun. Search 2(5):172

Taylor K (2001) Summarizing multiple aspects of model performance in a single diagram. Journal of Geophysical Research 106:7183–7192

Turner J, Parisi AV (2018) Ultraviolet radiation albedo and reflectance in review: The influence to ultraviolet exposure in occupational settings. International Journal of Environmental Research and Public Health 15. URL https://api.semanticscholar.org/CorpusID:51677009

Čížková K, Láska K, Metelka L, et al (2018) Reconstruction and analysis of erythemal uv radiation time series from hradec králové (czech republic) over the past 50 years. Atmospheric Chemistry and Physics 18(3):1805–1818. https://doi.org/10.5194/acp-18-1805-2018, URL https://acp.copernicus.org/articles/18/1805/2018/

Webb AR, Slaper H, Koepke P, et al (2011) Know Your Standard: Clarifying the CIE Erythema Action Spectrum. Photochemistry and Photobiology 87:483–486

World Health Organization (2002) Global Solar UV Index: A Practical Guide. URL https://www.who.int/publications/i/item/9241590076, accessed: April 2024

Declarations.

Declarations

Ethics approval and consent to participate: Not applicable.
Consent for publication: Not applicable.
Competing interests: The authors declare that they have no competing interests.
Funding: A. Laguarda acknowledges the *Programa de Desarrollo de las Ciencias Básicas, Udelar (PEDECIBA)* for funding support under the *"Despegue Científico"* program.
Availability of data and materials: The datasets generated and/or analyzed during the current study are not publicly available due to data ownership restrictions and confidentiality agreements. However, they are available from the corresponding author upon reasonable request and with the approval of the respective data owners.